



Article

# Supercurrent in Bi<sub>4</sub>Te<sub>3</sub> Topological Material-Based Three-Terminal Junctions

Jonas Kölzer <sup>1,2</sup>, Abdur Rehman Jalil <sup>1,2</sup>, Daniel Rosenbach <sup>1,2,†</sup>, Lisa Arndt <sup>3</sup>, Gregor Mussler <sup>1,2</sup>, Peter Schüffelgen <sup>1,2</sup>, Detlev Grützmacher <sup>1,2</sup>, Hans Lüth <sup>1,2</sup> and Thomas Schäpers <sup>1,2,\*</sup>

- Peter Grünberg Institute (PGI-9), Forschungszentrum Jülich, Wilhelm-Johnen-Straße, 52425 Jülich, Germany
- JARA-Fundamentals of Future Information Technology, Jülich-Aachen Research Alliance, Forschungszentrum Jülich and RWTH Aachen University, 52425 Jülich, Germany
- JARA Institute for Quantum Information, RWTH Aachen University, 52056 Aachen, Germany
- \* Correspondence: th.schaepers@fz-juelich.de
- † Current address: Physics Institute II, University of Cologne, Zülpicher Str. 77, 50937 Köln, Germany.

**Abstract:** In this paper, in an in situ prepared three-terminal Josephson junction based on the topological insulator  $Bi_4Te_3$  and the superconductor Nb the transport properties are studied. The differential resistance maps as a function of two bias currents reveal extended areas of Josephson supercurrent, including coupling effects between adjacent superconducting electrodes. The observed dynamics for the coupling of the junctions is interpreted using a numerical simulation of a similar geometry based on a resistively and capacitively shunted Josephson junction model. The temperature dependency indicates that the device behaves similar to prior experiments with single Josephson junctions comprising topological insulators' weak links. Irradiating radio frequencies to the junction, we find a spectrum of integer Shapiro steps and an additional fractional step, which is interpreted with a skewed current–phase relationship. In a perpendicular magnetic field, we observe Fraunhofer-like interference patterns in the switching currents.

**Keywords:** topological insulator; selective-area growth; molecular beam epitaxy; Josephson junction; three-terminal junction; Shapiro steps



Citation: Kölzer, J.; Jalil, A.R.; Rosenbach, D.; Arndt, L.; Mussler, G.; Schüffelgen, P.; Grützmacher, D.; Lüth, H.; Schäpers, T. Supercurrent in Bi<sub>4</sub>Te<sub>3</sub> Topological Material-Based Three-Terminal Junctions. *Nanomaterials* **2023**, *13*, 293. https:// doi.org/10.3390/nano13020293

Academic Editor: Zhidong Zhang

Received: 18 December 2022 Revised: 3 January 2023 Accepted: 4 January 2023 Published: 10 January 2023



Copyright: © 2023 by the authors. Licensee MDPI, Basel, Switzerland. This article is an open access article distributed under the terms and conditions of the Creative Commons Attribution (CC BY) license (https://creativecommons.org/licenses/by/4.0/).

# 1. Introduction

Hybrid structures comprising three-dimensional topological insulator nanoribbons combined with superconductors are a very promising platform for realizing circuits for fault-tolerant topological quantum computing [1–4]. For its operation, Majorana bound states are employed, which are formed by aligning an external magnetic field with a nanoribbon proximitized with an s-type superconductor [5–7]. For braiding, i.e., the exchange of Majorana states in nanoribbon networks, multi-terminal structures are required [2,8,9]. Braiding is an essential process in topological quantum computation. It can be performed by adjusting the superconducting phase of the superconducting electrodes to each other.

Multi-terminal Josephson junctions are the backbone of the Majorana braiding mechanism in a topological qubit, where a three-terminal Josephson junction acts as a basic building block [2]. Understanding the superconducting transport in such a device holds a key importance for the realization of a topological quantum system. Generally, the use of hybrid devices with multiple connections leads to rich physics in terms of transport properties. Indeed, theoretical studies have investigated singularities, such as Weyl nodes, in the Andreev spectra of multi-terminal Josephson junctions [10–12]. Moreover, multi-terminal Josephson junctions with topologically trivial superconducting leads may lead to realizations where the junction itself can be regarded as an artificial topological material [13]. Furthermore, three-terminal junctions also allow transport via the quartet mechanism and non-local Andreev processes by pairs of correlated Cooper pairs [14–18].

Nanomaterials **2023**, 13, 293

On the experimental side, multi-terminal Josephson junctions were fabricated with different materials for the weak link. In three-terminal Josephson junctions with a Cu or InAs nanowire subgap states [19,20] and half-integer Shapiro steps [21] were observed, indicating transport via quartets of entangled Cooper pairs. Supercurrent flow affected by dissipative currents in an adjacent junction was studied on graphene-based junctions [22]. Moreover, the higher-dimensional phase space was found to lead to fractional Shapiro steps in this type of junctions due to the inverse AC Josephson effect [23]. By combining a multi-terminal junction with a top gate, the effect of gate voltage and magnetic field on the critical current contour was studied [24–26]. Recently, flakes of the topological insulator Bi<sub>2</sub>Se<sub>3</sub> were also used as a weak link in an interferometer structure and evidence for a non-sinusoidal current–phase relationship was observed [27]. In flux-controlled three-terminal junctions based on Bi<sub>2</sub>Te<sub>3</sub>, the opening and closing of a minigap was studied using normal probes [28].

Here, we report on the transport properties of a three-terminal Josephson junction based on the Bi<sub>4</sub>Te<sub>3</sub> material system as the weak link and Nb as the superconductor. To fabricate the samples, we used selective-area growth for the Bi<sub>4</sub>Te<sub>3</sub> layer in combination with in situ bridge technology to define the superconducting electrodes [29]. Bi<sub>4</sub>Te<sub>3</sub> is a natural superlattice of alternating Bi<sub>2</sub> bilayers and Bi<sub>2</sub>Te<sub>3</sub> quintuple layers. Initially, Bi<sub>4</sub>Te<sub>3</sub> was reported to be a semimetal with zero band gap and a Dirac cone at the  $\Gamma$  point [30]. However, recent band structure calculations in conjunction with scanning tunneling spectroscopy and angular photoemission spectroscopy measurements suggest that the material is a semimetal with topological surface states [31–33]. In particular, advanced GW-band structure calculations have shown that a band gap of about  $0.2 \, \text{eV}$  opens at the  $\Gamma$  point, which significantly reduces the density of the bulk state in this energy range [33]. Bi<sub>4</sub>Te<sub>3</sub> is classified as a dual topological insulator, a strong topological insulator with a non-zero mirror Chern number, i.e., a topological crystalline insulator phase. However, in contrast to other three-dimensional topological insulators, i.e., Bi<sub>2</sub>Se<sub>3</sub> [34], a small area exists in the bulk band structure where a narrow electron pocket remains at the Fermi level [33]. Though Bi<sub>4</sub>Te<sub>3</sub> does not exhibit the proposed Dirac semimetal phase, it is still a very interesting material as it resides in close proximity to the critical point of band crossing in the topological phase diagram of  $Bi_xTe_y$  alloys [35]. Such a transition is proposed by Yang et al. [36] where a topological crystalline insulator (Bi<sub>2</sub>Te<sub>3</sub>) [37] can be topologically transformed into a topological Dirac semimetal through alloying it with other materials. On our multi-terminal junctions, we first investigated the DC properties and related the results to simulations based on the resistively and capacitively shunted Josephson junction model. We then measured the radio frequency (rf) response, finding evidence for coupling of adjacent junctions. Finally, the behavior of our three-terminal junctions when an out-of-plane magnetic field is applied is investigated.

#### 2. Materials and Methods

Using the previously introduced technologies of topological insulator selective-area growth and in situ bridge technology, we fabricated three-terminal Josephson junctions, as illustrated in Figure 1a [29,38]. The geometry of the nanoribbon T-shaped junction for selective-area growth is defined by trenches in a  $SiO_2/Si_3N_4$  (5 nm/15 nm) layer on a highly resistive Si (111) substrate [39]. First, the 600 nm-wide nanotrenches are etched into the top  $Si_3N_4$  layer using a combination of electron beam lithography and reactive ion etching. Subsequently, a second set of layers, i.e., a 100 nm-thick  $SiO_2$  layer and a 300 nm-thick  $Si_3N_4$  layer, is deposited on top to define the stencil mask for the in situ Nb deposition [29]. After patterning the structures for the stencil mask into  $Si_3N_4$ ,  $SiO_2$  is etched in hydrofluoric acid (HF) forming the free-hanging bridge structures. Simultaneously, the Si(111) surface in the selective-area growth trenches is released in the bottom  $SiO_2$  layer defined by the  $Si_3N_4$  layer on top. The  $Si_4Te_3$  layer is selectively grown within these trenches, while the  $Si_3N_4$  bridge structures are employed to define the geometry of the in situ deposited superconducting electrodes [29]. The  $Si_4Te_3$  layer is grown at a temperature of 310 °C using

Nanomaterials **2023**, 13, 293 3 of 12

molecular beam epitaxy. Subsequently, the 50 nm-thick superconducting Nb electrodes are deposited via electron beam evaporation followed by covering the whole structure with a 5 nm-thick Al<sub>2</sub>O<sub>3</sub> dielectric capping layer. Our processing scheme ensured a high-quality crystalline topological insulator material with clean superconductor interfaces [29,40], as reported in previous transmission electron microscopy studies. An electron microscopy image of the investigated device is presented in Figure 1b.

The measurements of the three-terminal Josephson junction were carried out in a dilution refrigerator with base temperature of  $T=25\,\mathrm{mK}$ . containing a 1-1-6 T vector magnet. As indicated in Figure 1b, the left, right and bottom junction electrodes are labeled "L", "R" and "B", respectively. Two current sources supply currents  $I_{\mathrm{LB}}$  and  $I_{\mathrm{RB}}$  from L and R to the bottom electrode, respectively, with the according voltages  $V_{\mathrm{LB}}$  and  $V_{\mathrm{RB}}$  measured. The differential resistances are measured by adding an AC current of 10 nA to the DC current bias using a lock-in amplifier. The rf-irradiation for the Shapiro step measurements was provided via an antenna placed in close vicinity to the sample.

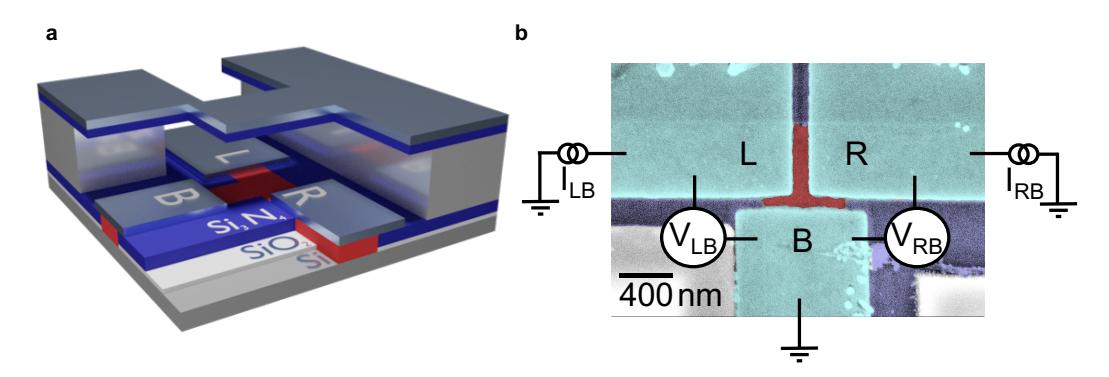


**Figure 1.** Rendering of a selective-area grown three-terminal Josephson junction and false color scanning electron micrograph with circuit: (a) The three-terminal junction is composed of the silicon substrate (gray bottom layer), the first hard mask composed out of a silicon oxide (white)/silicon nitride (blue) layer (as indicated by the labels). On top of this, another hard mask layer composed of silicon oxide (white) and silicon nitride (blue) is deposited and patterned as a shadow mask. The topological insulator (red) is grown selectively into the first hard mask trench and the shadow mask is used for the definition of the junction in the metal deposition (silver) step. (b) False-color scanning electron micrograph of the in situ prepared three-terminal junction device. Niobium contacts (cyan) are deposited on top of the TI (red). The measurement configuration is also indicated.

#### 3. Results and Discussion

#### 3.1. DC Characteristics

Information about the basic junction characteristics is obtained by measuring the differential resistances  $R_{\rm LB} = \Delta V_{\rm LB}/\Delta I_{\rm LB}$  and  $R_{\rm RB} = \Delta V_{\rm RB}/\Delta I_{\rm RB}$  as a function of the bias currents  $I_{\rm LB}$  and  $I_{\rm RB}$ , respectively. Starting with the left junction, we find that  $R_{\rm LB}$  shown in Figure 2a,b contains a superconducting region in the center when  $I_{\rm LB}$  and  $I_{\rm RB}$  are varied. The observed critical current contour is similar to what has been observed in induced superconducting nano-junctions made of high mobility materials such as InAs/Al [24,25] or graphene [22].

Nanomaterials **2023**, 13, 293 4 of 12

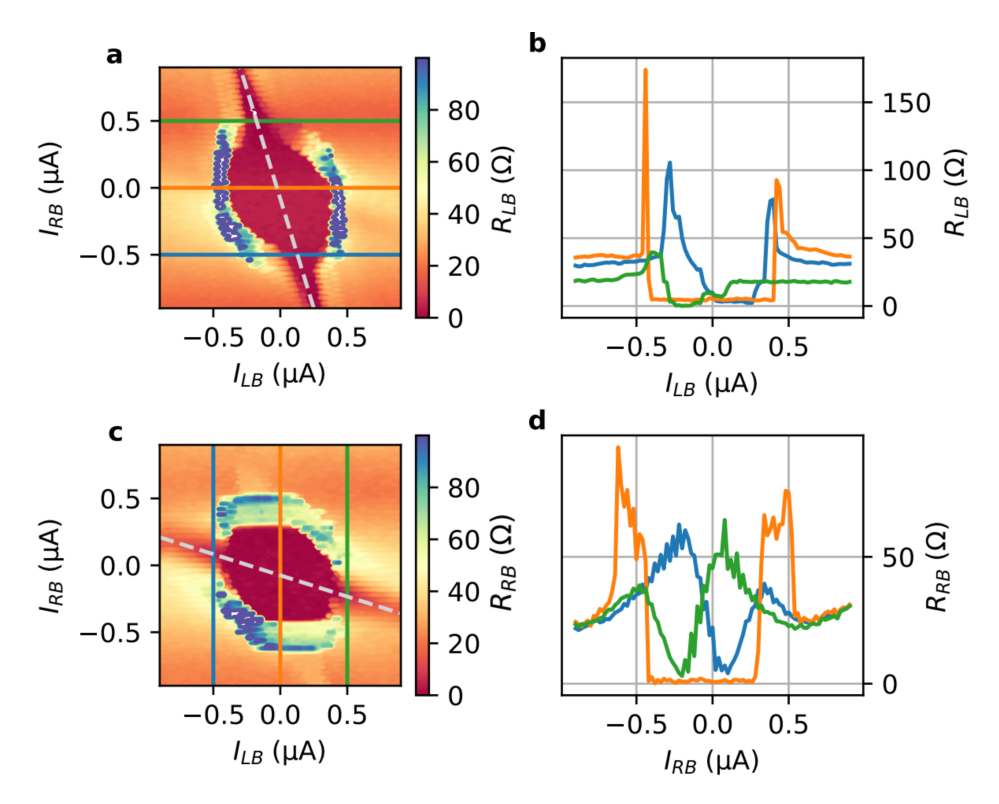


Figure 2. Differential resistance maps: (a)  $R_{\rm LB}$  as a function of the bias currents  $I_{\rm LB}$  and  $I_{\rm RB}$  at 25 mK with corresponding line cuts given in (b). In (c), the differential resistance map of  $R_{\rm RB}$  is depicted with a selection of line cuts given in (d). The dashed lines in (a,c) indicate the superconducting regions of compensating bias currents. The differential resistances were measured using the lock-in technique, i.e.,  $R_{\rm LB} = \Delta V_{\rm LB}/\Delta I_{\rm LB}$  and  $R_{\rm RB} = \Delta V_{\rm RB}/\Delta I_{\rm RB}$ .

The superconducting region extends along an inclined line indicated by the dashed line in Figure 2a. The switching to the superconducting state can be seen in the line cuts at fix values  $I_{RB}=0$  and  $\pm 0.7~\mu A$  provided in Figure 2b. The extension of the superconducting state originates from a part of  $I_{RB}$  which flows via R to L through the junction between L and B, compensating the current  $I_{LR}$  partly and thereby reducing the total current. For our three-terminal device, no reduced differential resistance is observed along the line  $I_{\rm LB}=I_{\rm RB}$ , which would indicate the presence of a Josephson supercurrent between the junction formed between electrodes L and R [24,26]. We attribute this to the fact that the distance between these electrodes is slightly larger than for the other junctions, so that no Josephson supercurrent is obtained. However, the junction between L and R acts as a shunt resistor taking care that the switching to the superconducting state is non-hysteretic. The differential resistance R<sub>RB</sub> measured between R and B electrodes, depicted in Figure 2c,d, shows behaviour similar to  $R_{LB}$ , i.e., featuring also an extended superconducting range due a compensation provided by part of ILR. The tilt of the superconducting range indicated by the dashed line in Figure 2c is lower compared to Figure 2a since now  $I_{LR}$  is the compensating current.

## 3.2. Simulations

The experimental results are modeled by assuming a network of two resistively and capacitively shunted Josephson (RCSJ) junctions coupled by a resistor  $R_C$ , as illustrated in Figure 3a. Solving the related system of differential equations numerically, in analogy to what was presented in previous works [23,24], we simulate the behaviour of the experimental system (for information about the procedure, see the Supplementary Material: Supplementary Note 3). The results of the simulations are shown in Figure 3b–e, where the differential resistance  $R_{\rm LB}$  is given as a function of the bias currents  $I_{\rm LB}$  and  $I_{\rm RB}$ .

Nanomaterials **2023**, 13, 293 5 of 12

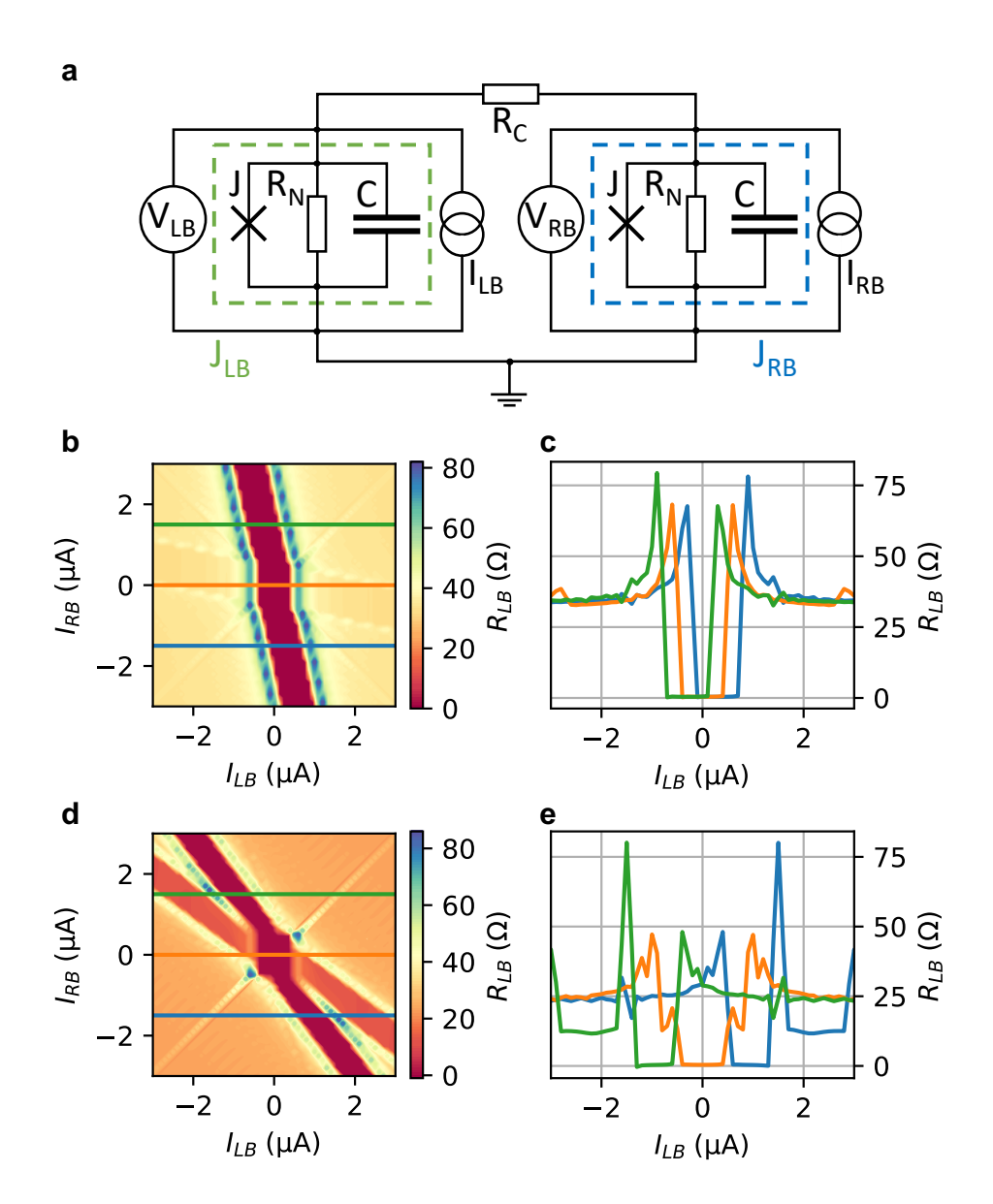


**Figure 3.** Numerical simulation of different coupling scenarios: (a) The three-terminal circuit is modeled by two resistively and capacitively shunted Josephson junctions  $J_{LB}$  and  $J_{RB}$  (green and blue dashed line boxes), which are each modeled by a resistor  $R_N$ , a capacitor C and an ideal Josephson junction J. Currents  $I_{LB}$  and  $I_{RB}$  are supplied via current sources, while the voltage drops  $V_{LB}$  and  $V_{RB}$  across the junctions are measured. Both junctions are coupled via a coupling resistance  $R_C$ . (b) Differential resistance  $R_{LB}$  as a function of current biases for a realistic scenario for  $R_C$  close to the one extracted in the experiment:  $R_N = 40 \,\Omega$ ,  $R_C = 160 \,\Omega$ ,  $I_C = 538 \,\mathrm{nA}$ ,  $\beta_C = (2e/\hbar) I_C R_N^2 C = 0.1$ . The zero resistance range is observed as a tilted line due to compensation by a part of  $I_{RB}$ . Additionally, the influence of the second junction is observed as a similar line close to horizontal orientation. The corresponding line cuts indicated in (b) are presented in (c). The scenario for a very small coupling resistance  $(R_C \to 0)$  is shown as a color map of  $R_{LB}$  and selected line cuts in (d,e).

The model describes the experiment well by reproducing the Josephson supercurrent along the inclined lines originating from compensating currents from both electrodes with a superconducting region at the center. The inclination is determined by the coupling resistance  $R_C$ . In Figure 3b,c, the coupling resistance was taken as  $R_C = 4 \cdot R_{LB}$ , with  $R_{LB} = 40 \,\Omega$  which results in the same tilt as observed experimentally. Taking these values into account, the normal state resistance is given by  $R_N = 6/5 \cdot R_{LB} = 48 \,\Omega$ . In our simulations, for the critical current and for the Steward–McCumber parameter we

Nanomaterials 2023, 13, 293 6 of 12

assumed  $I_c = 538 \,\text{nA}$  and  $\beta_c = (2e/\hbar)I_cR_N^2C = 0.1$ , respectively, with C being the junction capacitance. We found that the superconducting state in the junction between R and B leads to some weak feature as a similar line inclined towards horizontal orientation. Note that for this line  $R_{LB}$  is non-zero, as the supercurrent in the other junction only partly reduces the current in the junction between L and B and hence only partially reduces the voltage drop. A noticeable difference between experiment and simulation is that in the measurements the extension of the superconducting state observed along the inclined line (cf. Figure 2a) is decreased compared to the simulation depicted in Figure 3b. As discussed by Draelos et al. [22], this effect can be explained by dissipation in the neighboring junction being in the normal state, resulting in an effective heating, in particular for junctions with small dimensions. In our simulation, the direct coupling between the different junctions was neglected. As shown by Arnault et al. [23], including coupling results in a more complex contour of the critical current area. If the coupling resistance becomes very small, i.e.,  $R_C \rightarrow 0$ , the observed lines in the differential resistance shift towards the diagonal (cf. Figure 3d,e). Thus, both junctions are maximally correlated to both current biases  $I_{LB}$ and  $I_{RB}$ .

#### 3.3. Temperature Dependence

In Figure 4a–f, the differential resistance maps are shown for  $R_{LB}$  and  $R_{RB}$  measured at temperatures of 100 mK, 200 mK and 800 mK.

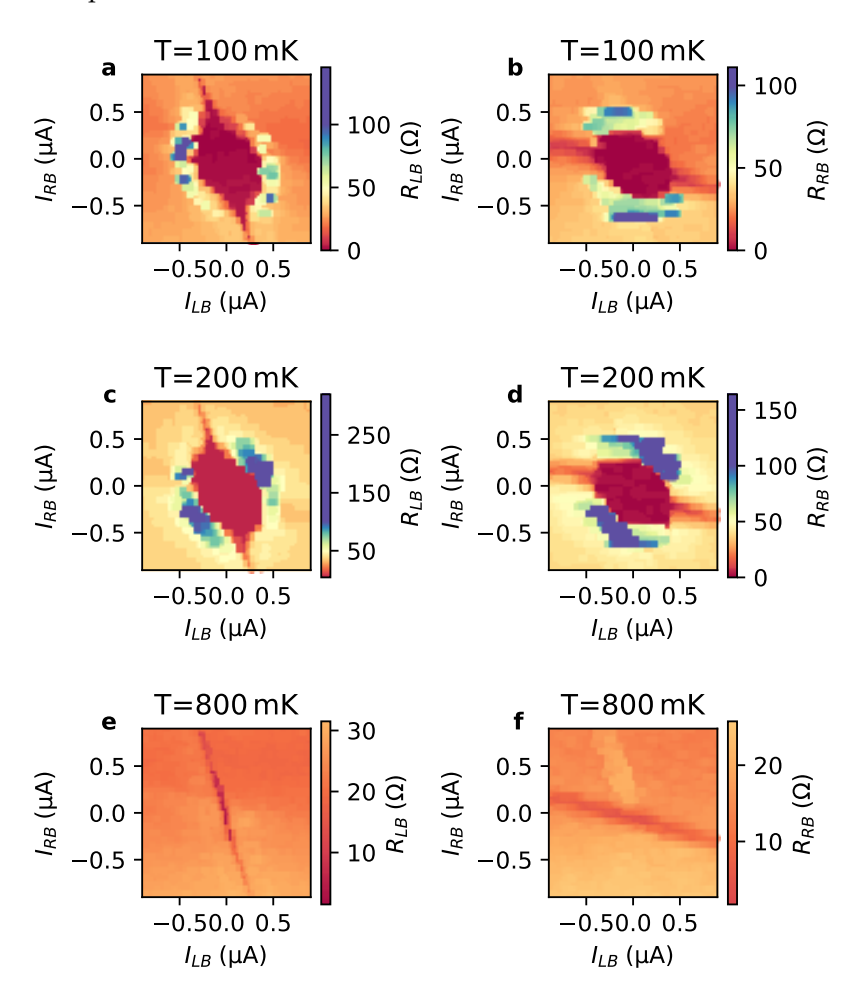


**Figure 4.** Differential resistance maps at various temperatures: Left column ( $\mathbf{a}$ , $\mathbf{c}$ , $\mathbf{e}$ ) shows the differential resistance  $R_{LB}$ , right column ( $\mathbf{b}$ , $\mathbf{d}$ , $\mathbf{f}$ )  $R_{RB}$ , accordingly. The temperatures displayed in the rows from top to bottom are  $100 \, \text{mK}$ ,  $200 \, \text{mK}$  and  $800 \, \text{mK}$ .

Nanomaterials 2023. 13, 293 7 of 12

One finds that with increasing temperature the area of the central superconducting region shrinks. This is in accordance with the temperature dependence of the critical current of a single  $Nb/Bi_4Te_3/Nb$  reference junction, as shown in the Supplementary Material: Supplementary Figure S1. It is noteworthy that the superconducting feature along the inclined lines basically does not change with increasing temperature. This can be explained by the fact that the dissipation in the neighboring junction already leads to an increased temperature larger than the substrate temperature.

#### 3.4. rf Characteristics

Next, the radio frequency response of the system is investigated in order to confirm that the experiment is described well by Josephson junction physics and to analyze the rf response of the Josephson current. This is done by first choosing a frequency and an amplitude for the rf irradiation so that both junctions show a large rf response in the differential resistance. Subsequently, the same DC bias sweeps are performed as in the prior experiments. Figure 5a,b show Shapiro step measurements of the differential resistances  $R_{\rm LB}$  and  $R_{\rm RB}$ , respectively, as a function of bias currents  $I_{\rm LB}$  and  $I_{\rm RB}$ . The differential resistances are calculated by numerical differentiation. Differential resistances obtained by lock-in amplifier measurements can be found in the Supplementary Material: Supplementary Figures S2 and S3.

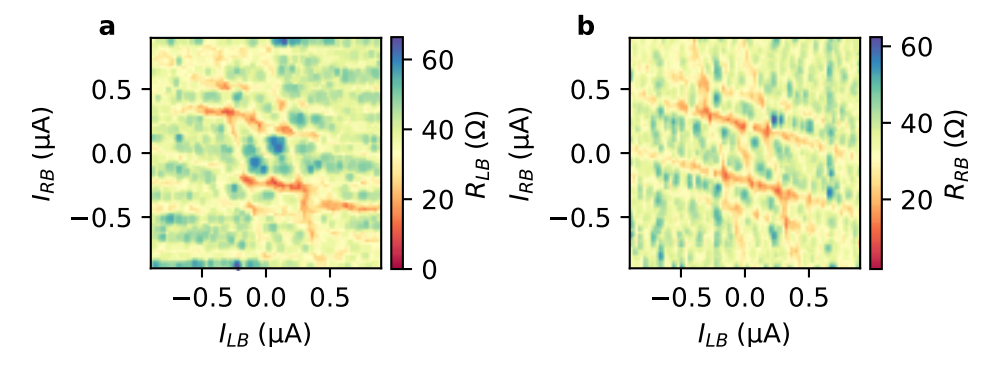


**Figure 5.** Shapiro step measurements at 5.8 GHz: (a) Numerically determined differential resistance  $R_{\rm LB}$  as a function of  $I_{\rm LB}$  and  $I_{\rm RB}$  at 5.8 GHz and rf power of 0 dBm. (b) Corresponding map of the differential resistance  $R_{\rm RB}$ .

The rf frequency  $f_{\rm rf}$  and the according power was set to 5.8 GHz and 0 dBm, respectively. The differential resistances show clear intercrossing stripe-like patterns which can be attributed to the presence of Shapiro steps, confirming the presence of a Josephson supercurrent. The intercrossing parallel stripes indicate a coupling of both junctions. By calculating the related voltage drop, we find that for both junctions the Shapiro steps are located at integer multiples,  $n=1,2,3\ldots$ , of the characteristic voltage  $V_0=hf_{\rm rf}/2e$ .

In Figure 6a,b, the differential resistance maps of  $R_{\rm LB}$  and  $R_{\rm LB}$ , now taken at 8.5 GHz at 0 dBm, are depicted, respectively. Here, the color maps are plotted as a function of the normalized voltages  $V_{\rm LB}/V_0$  and  $V_{\rm RB}/V_0$ . On first sight, one finds that the Shapiro step pattern is more pronounced in  $R_{\rm LB}$ . We attribute this to a stronger coupling of the rf signal compared to the neighbouring junction due to spatial variations in the rf field. As for the measurements at 5.8 GHz, a coupling of both junctions, although weaker, is observed. Our experimental results concerning Shapiro step measurements are supported by comparison to simulations based on the previously introduced RCSJ model. In Supplementary Figure S4a,b maps of the simulated values of  $R_{\rm LB}$  and  $R_{\rm LB}$  as a function of the normalized bias voltages are shown. There, one finds that the coupling by  $R_{\rm C}$  results in a weak cross coupling of the Shapiro signal, resulting in intercrossing stripe-like patterns of different contrast.

Nanomaterials **2023**, 13, 293 8 of 12

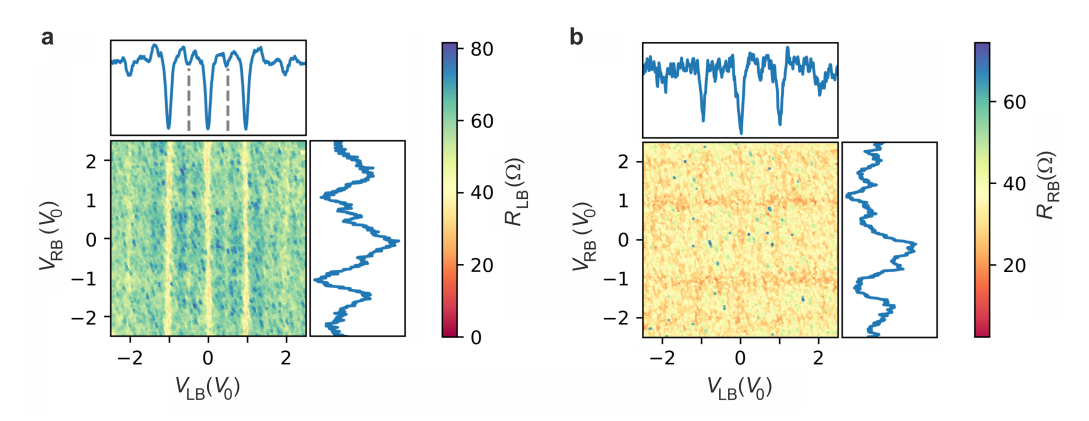


**Figure 6.** Shapiro step measurements at 8.5 GHz: (a) Numerically determined differential resistance  $R_{\rm LB}$  as a function of the normalized voltage drops  $V_{\rm LB}/V_0$  and  $V_{\rm RB}/V_0$  at 8.5 GHz and rf power of 0 dBm, with  $V_0 = h f_{\rm rf}/2e$ . The blue curves represent the averaged signal along  $V_{\rm LB}/V_0$  and  $V_{\rm RB}/V_0$ , respectively. The dashed lines indicate the half-integer steps. (b) Corresponding map of the differential resistance  $R_{\rm RB}$ .

A closer inspection of the resistance map presented in Figure 6a reveals that apart from the integer Shapiro steps half-integer Shapiro steps, e.g., at n = 1/2, are also observed. The half-integer steps are also clearly resolved in the averaged value of  $R_{\rm LB}$  along  $V_{\rm LB}/V_0$ shown in Figure 6a. In single Josephson junctions, such fractional steps are interpreted by assuming a skewed current-phase relationship [41-43] (a simulation for this case using our model is provided in the Supplementary Material). More specifically for multi-terminal junctions the rf response of superconductivity induced into normal metal was studied previously by Duvauchelle et al. [21]. Here, half-integer steps were found and interpreted as a feature due to the presence of coherent quartet states. However, in Figure 2 we did not find indications of quartet states, which would be visible by a feature in the differential resistance at opposite voltage drops on the left and right terminal [19]. Other experimental observations of such fractional steps in multi-terminal junctions are interpreted on the basis of highly connected nonlinear networks of Josephson junctions, where (due to the higher phase space) different transitions of the phase particle in the washboard potential are possible [23]. However, since fractional Shapiro steps were observed in single junctions made with similar materials [44], we favor the explanation based on a skewed currentphase relationship, which can be attributed to contributions of quasi-ballistic transport. Most likely, the quasi-ballistic transport takes place in the topologically protected surface states in Bi<sub>4</sub>Te<sub>3</sub>. In our measurements under rf radiation, we did not find indications of missing odd Shapiro steps, as predicted when Majorana bound states are present in topological junctions [29,45]. Probably, for our samples the narrow width of the Bi<sub>4</sub>Te<sub>3</sub> ribbons prevents the formation of these states, since due to the finite Berry phase a magnetic field along the junctions is required to gain a gap closure for the coherent surface states around the nanoribbon cross section [38]. The finite Berry phase of  $\pi$  accumulates because of the  $2\pi$  rotation of the spin as it goes around the surface of the topological insulator ribbon.

# 3.5. Magnetic Field Response

The junction characteristics were also analyzed in a perpendicularly oriented magnetic field  $B_{\perp}$ . In Figure 7a, the magnetic field dependence  $R_{\rm LB}$  is plotted as a function of  $B_{\perp}$  and  $I_{\rm LB}$ , while  $I_{\rm RB}$  is kept at zero. One clearly observes a Fraunhofer-like interference pattern of the switching current, i.e., the boundary between the red superconducting areas and the areas with finite resistance. The blue line in Figure 7a indicates the according fitting based on the Fraunhofer interference relation. The close resemblance of the experimental data to an ideal Fraunhofer pattern points towards a relatively homogeneous distribution of the supercurrent density. From the fit, we extract a period of about  $\Delta B = 14\,\mathrm{mT}$ , which corresponds to a junction area of  $152 \times 10^3\,\mathrm{nm}^2$ . Relating these values to the dimensions of the left junction  $J_{\rm LB}$ , one finds that the period is about a factor of ten smaller than

Nanomaterials **2023**, 13, 293 9 of 12

expected. Based on the actual junction size of  $200 \times 72 \,\mathrm{nm}^2$ , a period of  $144 \,\mathrm{mT}$  is expected for a h/2e flux periodicity. We attribute the discrepancy in the experimental period to a pronounced flux focusing effect, where the magnetic field is expelled from the edge regions of the superconducting electrodes and bundled in the junction area. As a matter of fact, a comparably large flux focusing effect was previously observed in similar planar Josephson junctions based on topological insulators and Nb superconducting electrodes [38].

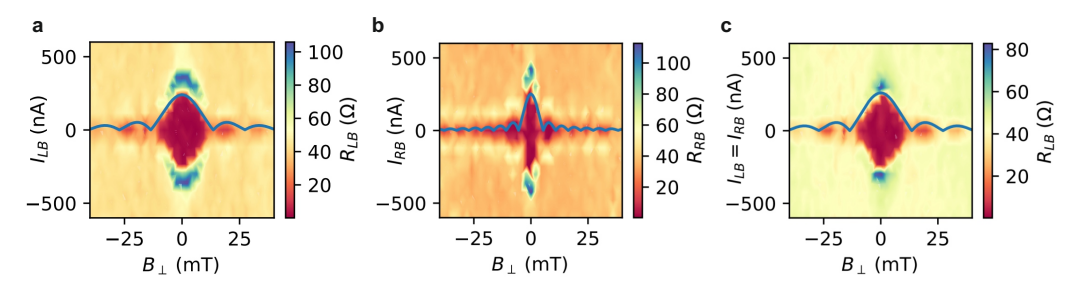


**Figure 7.** Differential resistances under perpendicular magnetic field sweep: (a) A map of  $R_{LB}$  as a function of  $B_{\perp}$  and  $I_{LB}$  for  $I_{RB} = 0$ . (b) The corresponding map of  $R_{RB}$  as a function of  $B_{\perp}$  and  $I_{RB}$  for  $I_{LB} = 0$ . In (c), the sweep current is chosen to be  $I_{LB} = I_{RB}$ , which corresponds to a sweep along the diagonal in the current plane. In all cases, a standard Fraunhofer pattern is fitted indicated as blue lines.

In Figure 7b, the magnetic field dependence  $R_{\rm RB}$  is shown as a function of  $B_{\perp}$  and  $I_{\rm RB}$  at  $I_{\rm LB}=0$ . Once again, a Fraunhofer-like interference is observed, although with a smaller period, i.e., a larger effective area where the magnetic flux is picked up. The reason for the difference compared to the measurements shown in Figure 7a might be some inhomogeneity in the supercurrent density in the junction. Finally, the  $R_{\rm LB}$  maps are scanned diagonally, i.e.,  $I_{\rm LB}=I_{\rm RB}$ , as shown in Figure 7c. Here, once again a regular Fraunhofer pattern is observed, which is almost identical to the pattern shown in Figure 7a, which is an indication that the current  $I_{\rm RB}$  through the neighboring junction basically has not effect on the left junction.

#### 4. Conclusions

We have succeeded in extending the previously developed in situ fabrication technology for Josephson junctions to a working and more complex design of a three-terminal junction. Analysis of the transport experiments shows that our system indeed behaves like a coupled network of Josephson junctions in DC transport, rf response, as well as magnetic field response. This is the first report on the topological multi-terminal devices where an interaction between the individual Josephson junctions is observed. Moreover, the observation of fractional steps in the rf response opens a window that provides a first insight into the novel physics of this type of device. We attribute the presence of fractional steps to quasi-ballistic transport in topologically protected surface states in Bi<sub>4</sub>Te<sub>3</sub>. Our interpretation is supported by recent band structure calculations predicting the presence of topological surface states. In these states, quasi-ballistic transport is likely owed to reduced backscattering [29]. Nevertheless, part of the supercurrent might also be transported by bulk carriers, which are always present in Bi<sub>4</sub>Te<sub>3</sub> due to the special band structure [33]. On a more technical level, our results demonstrate the realization of more complex devices required for network structures in topological quantum circuits.

Further investigations and detailed understanding of such a system are crucial for the realization of complex topological quantum systems. In future, similar experiments with more intricate circuit designs and superconducting phase controlled measurements will be performed. The complexities in the junction characteristics arose from the selected weak-link material  $Bi_4Te_3$ . In future experiments, we plan to incorporate conventional three-dimensional topological insulators, e.g.,  $Bi_2Te_3$ ,  $Sb_2Te_3$ ,  $Bi_2Se_3$  and the topological Dirac semimetal exhibited by the correctly tuned  $Bi_xTe_y$  stoichiometric alloy.

Nanomaterials 2023. 13, 293 10 of 12

**Supplementary Materials:** The following supporting information can be downloaded at: https://www.mdpi.com/article/10.3390/nano13020293/s1, Figure S1: Current voltage characteristics of a single Nb/Bi $_4$ Te $_3$ /Nb junction; Figure S2: Shapiro Step response at 5.8 GHz; Figure S3: Shapiro step response at 8.5 GHz; Figure S4: Shapiro step simulations at 8.5 GHz; Figure S5: Simulation of Shapiro maps at 8.5 GHz with  $2\phi$  term.

**Author Contributions:** Conceptualization, J.K., A.R.J. and T.S.; methodology, J.K., A.R.J. and G.M.; software, J.K. and L.A.; formal analysis, J.K. and T.S.; investigation, J.K., A.R.J., D.R.; writing—original draft preparation, J.K., A.R.J. and T.S.; writing—review and editing, J.K., A.R.J., D.R., P.S., D.G., H.L. and T.S.; supervision, T.S. All authors have read and agreed to the published version of the manuscript.

Funding: This work was partly funded by the Deutsche Forschungsgemeinschaft (DFG, German Research Foundation) under Germany's Excellence Strategy—Cluster of Excellence Matter and Light for Quantum Computing (ML4Q) EXC 2004/1—390534769, the German Federal Ministry of Education and Research (BMBF) via the Quantum Futur project "MajoranaChips" (Grant No. 13N15264) within the funding program Photonic Research Germany, as well as the Bavarian Ministry of Economic Affairs, Regional Development and Energy within Bavaria's High-Tech Agenda Project "Bausteine für das Quantencomputing auf Basis topologischer Materialien mit experimentellen und theoretischen Ansätzen" (grant allocation no. 07 02/686 58/1/21 1/22 2/23).

**Data Availability Statement:** The data presented in this study are openly available in JülichDATA at [https://doi.org/10.26165/JUELICH-DATA/QLJK8D], accessed on 3 January 2023.

**Acknowledgments:** We thank Herbert Kertz for technical assistance as well as Kristof Moors and Roman Riwar for fruitful discussions.

Conflicts of Interest: The authors declare no conflict of interest. The funders had no role in the design of the study; in the collection, analyses or interpretation of data; in the writing of the manuscript; or in the decision to publish the results.

#### Abbreviations

The following abbreviation is used in this manuscript:

RCSJ resistively and capacitively shunted junction

## References

- Kitaev, A. Fault-tolerant quantum computation by anyons. Ann. Phys. 2003, 303, 2–30. [CrossRef]
- 2. Hyart, T.; van Heck, B.; Fulga, I.C.; Burrello, M.; Akhmerov, A.R.; Beenakker, C.W.J. Flux-controlled quantum computation with Majorana fermions. *Phys. Rev. B* **2013**, *88*, 035121. [CrossRef]
- 3. Aasen, D.; Hell, M.; Mishmash, R.V.; Higginbotham, A.; Danon, J.; Leijnse, M.; Jespersen, T.S.; Folk, J.A.; Marcus, C.M.; Flensberg, K.; et al. Milestones Toward Majorana-Based Quantum Computing. *Phys. Rev. X* **2016**, *6*, 031016. [CrossRef]
- 4. Manousakis, J.; Altland, A.; Bagrets, D.; Egger, R.; Ando, Y. Majorana qubits in a topological insulator nanoribbon architecture. *Phys. Rev. B* **2017**, *95*, 165424. [CrossRef]
- 5. Cook, A.; Franz, M. Majorana fermions in a topological-insulator nanowire proximity-coupled to an *s*-wave superconductor. *Phys. Rev. B* **2011**, *84*, 201105. [CrossRef]
- 6. Cook, A.M.; Vazifeh, M.M.; Franz, M. Stability of Majorana fermions in proximity-coupled topological insulator nanowires. *Phys. Rev. B* **2012**, *86*, 155431. [CrossRef]
- Legg, H.F.; Loss, D.; Klinovaja, J. Majorana bound states in topological insulators without a vortex. Phys. Rev. B 2021, 104, 165405.
  [CrossRef]
- 8. Fu, L.; Kane, C.L. Superconducting Proximity Effect and Majorana Fermions at the Surface of a Topological Insulator. *Phys. Rev. Lett.* **2008**, *100*, 096407. [CrossRef]
- 9. Stenger, J.P.T.; Hatridge, M.; Frolov, S.M.; Pekker, D. Braiding quantum circuit based on the  $4\pi$  Josephson effect. *Phys. Rev. B* **2019**, 99, 035307. [CrossRef]
- 10. Yokoyama, T.; Nazarov, Y.V. Singularities in the Andreev spectrum of a multiterminal Josephson junction. *Phys. Rev. B* **2015**, 92, 155437. [CrossRef]
- 11. Eriksson, E.; Riwar, R.P.; Houzet, M.; Meyer, J.S.; Nazarov, Y.V. Topological transconductance quantization in a four-terminal Josephson junction. *Phys. Rev. B* **2017**, *95*, 075417. [CrossRef]
- 12. Xie, H.Y.; Vavilov, M.G.; Levchenko, A. Weyl nodes in Andreev spectra of multiterminal Josephson junctions: Chern numbers, conductances and supercurrents. *Phys. Rev. B* **2018**, *97*, 035443. [CrossRef]

Nanomaterials 2023, 13, 293 11 of 12

13. Riwar, R.P.; Houzet, M.; Meyer, J.S.; Nazarov, Y.V. Multi-terminal Josephson junctions as topological matter. *Nat. Commun.* **2016**, 7, 11167. [CrossRef] [PubMed]

- 14. Houzet, M.; Samuelsson, P. Multiple Andreev reflections in hybrid multiterminal junctions. Phys. Rev. B 2010, 82, 060517. [CrossRef]
- 15. Freyn, A.; Douçot, B.; Feinberg, D.; Mélin, R. Production of Nonlocal Quartets and Phase-Sensitive Entanglement in a Superconducting Beam Splitter. *Phys. Rev. Lett.* **2011**, *106*, 257005. [CrossRef] [PubMed]
- 16. Nowak, M.P.; Wimmer, M.; Akhmerov, A.R. Supercurrent carried by nonequilibrium quasiparticles in a multiterminal Josephson junction. *Phys. Rev. B* **2019**, *99*, 075416. [CrossRef]
- 17. Melo, A.; Fatemi, V.; Akhmerov, A.R. Multiplet supercurrent in Josephson tunneling circuits. SciPost Phys. 2022, 12, 17. [CrossRef]
- 18. Huang, K.F.; Ronen, Y.; Mélin, R.; Feinberg, D.; Watanabe, K.; Taniguchi, T.; Kim, P. Evidence for 4e charge of Cooper quartets in a biased multi-terminal graphene-based Josephson junction. *Nat. Commun.* **2022**, *13*, 3032. [CrossRef]
- 19. Pfeffer, A.H.; Duvauchelle, J.E.; Courtois, H.; Mélin, R.; Feinberg, D.; Lefloch, F. Subgap structure in the conductance of a three-terminal Josephson junction. *Phys. Rev. B* **2014**, *90*, 075401. [CrossRef]
- 20. Cohen, Y.; Ronen, Y.; Kang, J.H.; Heiblum, M.; Feinberg, D.; Mélin, R.; Shtrikman, H. Nonlocal supercurrent of quartets in a three-terminal Josephson junction. *Proc. Natl. Acad. Sci. USA* **2018**, *115*, 6991–6994. [CrossRef]
- 21. Duvauchelle, J.E.; Pfeffer, A.H.; Courtois, H.; Lefloch, F. Quantum Coherence of the Quartet Scheme Observed by Shapiro Resonance Under Radio-Frequency Irradiation in Three Terminal Josephson Junctions. *IEEE Trans. Appl. Supercond.* **2016**, 26, 1–4. [CrossRef]
- 22. Draelos, A.W.; Wei, M.T.; Seredinski, A.; Li, H.; Mehta, Y.; Watanabe, K.; Taniguchi, T.; Borzenets, I.V.; Amet, F.; Finkelstein, G. Supercurrent Flow in Multiterminal Graphene Josephson Junctions. *Nano Lett.* **2019**, *19*, 1039–1043. [CrossRef]
- 23. Arnault, E.G.; Larson, T.F.Q.; Seredinski, A.; Zhao, L.; Idris, S.; McConnell, A.; Watanabe, K.; Taniguchi, T.; Borzenets, I.; Amet, F.; et al. Multiterminal Inverse AC Josephson Effect. *Nano Lett.* **2021**, *21*, 9668–9674. [CrossRef]
- 24. Graziano, G.V.; Lee, J.S.; Pendharkar, M.; Palmstrøm, C.J.; Pribiag, V.S. Transport studies in a gate-tunable three-terminal Josephson junction. *Phys. Rev. B* **2020**, *101*, 054510. [CrossRef]
- 25. Pankratova, N.; Lee, H.; Kuzmin, R.; Wickramasinghe, K.; Mayer, W.; Yuan, J.; Vavilov, M.G.; Shabani, J.; Manucharyan, V.E. Multiterminal Josephson Effect. *Phys. Rev. X* **2020**, *10*, 031051. [CrossRef]
- Graziano, G.V.; Gupta, M.; Pendharkar, M.; Dong, J.T.; Dempsey, C.P.; Palmstrøm, C.; Pribiag, V.S. Selective Control of Conductance Modes in Multi-terminal Josephson Junctions. arXiv 2022, arXiv:2201.01373.
- 27. Kurter, C.; Finck, A.; Hor, Y.S.; Van Harlingen, D.J. Evidence for an anomalous current–phase relation in topological insulator Josephson junctions. *Nat. Commun.* **2015**, *6*, 7130. [CrossRef]
- 28. Yang, G.; Lyu, Z.; Wang, J.; Ying, J.; Zhang, X.; Shen, J.; Liu, G.; Fan, J.; Ji, Z.; Jing, X.; et al. Protected gap closing in Josephson trijunctions constructed on Bi<sub>2</sub>Te<sub>3</sub>. *Phys. Rev. B* **2019**, *100*, 180501. [CrossRef]
- 29. Schüffelgen, P.; Rosenbach, D.; Li, C.; Schmitt, T.W.; Schleenvoigt, M.; Jalil, A.R.; Schmitt, S.; Kölzer, J.; Wang, M.; Bennemann, B.; et al. Selective area growth and stencil lithography for in situ fabricated quantum devices. *Nat. Nanotechnol.* **2019**, *14*, 825–831. [CrossRef]
- 30. Saito, Y.; Fons, P.; Makino, K.; Mitrofanov, K.V.; Uesugi, F.; Takeguchi, M.; Kolobov, A.V.; Tominaga, J. Compositional tuning in sputter-grown highly oriented Bi–Te films and their optical and electronic structures. *Nanoscale* **2017**, *9*, 15115–15121. [CrossRef] [PubMed]
- 31. Chagas, T.; Ribeiro, G.A.S.; Gonçalves, P.H.R.; Calil, L.; Silva, W.S.; Malachias, Â.; Mazzoni, M.S.C.; Magalhães-Paniago, R. Bi<sub>2</sub>:Bi<sub>2</sub>Te<sub>3</sub> stacking influence on the surface electronic response of the topological insulator Bi<sub>4</sub>Te<sub>3</sub>. *Electron. Struct.* **2020**, *2*, 015002. [CrossRef]
- 32. Chagas, T.; Ashour, O.A.; Ribeiro, G.A.S.; Silva, W.S.; Li, Z.; Louie, S.G.; Magalhães Paniago, R.; Petroff, Y. Multiple strong topological gaps and hexagonal warping in Bi<sub>4</sub>Te<sub>3</sub>. *Phys. Rev. B* **2022**, *105*, L081409. [CrossRef]
- 33. Nabok, D.; Tas, M.; Kusaka, S.; Durgun, E.; Friedrich, C.; Bihlmayer, G.; Blügel, S.; Hirahara, T.; Aguilera, I. Bulk and surface electronic structure of Bi<sub>4</sub>Te<sub>3</sub> from *GW* calculations and photoemission experiments. *Phys. Rev. Mater.* **2022**, *6*, 034204. [CrossRef]
- 34. Michiardi, M.; Aguilera, I.; Bianchi, M.; de Carvalho, V.E.; Ladeira, L.O.; Teixeira, N.G.; Soares, E.A.; Friedrich, C.; Blügel, S.; Hofmann, P. Bulk band structure of Bi<sub>2</sub>Te<sub>3</sub>. *Phys. Rev. B* **2014**, *90*, 075105. [CrossRef]
- 35. Jalil, A.R. Engineering Topological Superlattices and Their Epitaxial Integration in Selectively Grown Hybrid Nanostructures via MBE. Ph.D. Thesis, RWTH Aachen University, Aachen, Germany, 2022. [CrossRef]
- 36. Yang, B.J.; Nagaosa, N. Classification of stable three-dimensional Dirac semimetals with nontrivial topology. *Nat. Commun.* **2014**, 5, 4898. [CrossRef] [PubMed]
- 37. Rauch, T.c.v.; Flieger, M.; Henk, J.; Mertig, I.; Ernst, A. Dual Topological Character of Chalcogenides: Theory for Bi<sub>2</sub>Te<sub>3</sub>. *Phys. Rev. Lett.* **2014**, *112*, 016802. [CrossRef] [PubMed]
- 38. Rosenbach, D.; Schmitt, T.W.; Schüffelgen, P.; Stehno, M.P.; Li, C.; Schleenvoigt, M.; Jalil, A.R.; Mussler, G.; Neumann, E.; Trellenkamp, S.; et al. Reappearance of first Shapiro step in narrow topological Josephson junctions. *Sci. Adv.* **2021**, *7*, eabf1854. [CrossRef]
- 39. Schmitt, T.W.; Connolly, M.R.; Schleenvoigt, M.; Liu, C.; Kennedy, O.; Chávez-Garcia, J.M.; Jalil, A.R.; Bennemann, B.; Trellenkamp, S.; Lentz, F.; et al. Integration of topological insulator Josephson junctions in superconducting qubit circuits. *Nano Lett.* 2022, 22, 2595–2602. [CrossRef]

Nanomaterials **2023**, 13, 293

40. Kölzer, J.; Moors, K.; Jalil, A.R.; Zimmermann, E.; Rosenbach, D.; Kibkalo, L.; Schüffelgen, P.; Mussler, G.; Grützmacher, D.; Schmidt, T.L.; et al. In-plane magnetic field-driven symmetry breaking in topological insulator-based three-terminal junctions. *Commun. Mater.* **2021**, *2*, 116. [CrossRef]

- 41. Snyder, R.A.; Trimble, C.J.; Rong, C.C.; Folkes, P.A.; Taylor, P.J.; Williams, J.R. Weak-link Josephson Junctions made from topological crystalline insulators. *Phys. Rev. Lett.* **2018**, *121*, 097701. [CrossRef]
- 42. Panghotra, R.; Raes, B.; de Souza Silva, C.C.; Cools, I.; Keijers, W.; Scheerder, J.E.; Moshchalkov, V.V.; Van de Vondel, J. Giant fractional Shapiro steps in anisotropic Josephson junction arrays. *Commun. Phys.* **2020**, *3*, 53. [CrossRef]
- 43. Raes, B.; Tubsrinuan, N.; Sreedhar, R.; Guala, D.S.; Panghotra, R.; Dausy, H.; de Souza Silva, C.C.; Van de Vondel, J. Fractional Shapiro steps in resistively shunted Josephson junctions as a fingerprint of a skewed current–phase relationship. *Phys. Rev. B* **2020**, *102*, 054507. [CrossRef]
- 44. Rosenbach, D. Quantum Transport and Induced Superconductivity in Selectively Deposited Topological Insulator Devices. Ph.D. Thesis, RWTH Aachen University, Aachen, Germany, 2021. [CrossRef]
- 45. Domínguez, F.; Kashuba, O.; Bocquillon, E.; Wiedenmann, J.; Deacon, R.S.; Klapwijk, T.M.; Platero, G.; Molenkamp, L.W.; Trauzettel, B.; Hankiewicz, E.M. Josephson junction dynamics in the presence of 2*π* and 4*π*-periodic supercurrents. *Phys. Rev. B* **2017**, 95, 195430. [CrossRef]

**Disclaimer/Publisher's Note:** The statements, opinions and data contained in all publications are solely those of the individual author(s) and contributor(s) and not of MDPI and/or the editor(s). MDPI and/or the editor(s) disclaim responsibility for any injury to people or property resulting from any ideas, methods, instructions or products referred to in the content.